



OPEN

Empirical evidence for multi-decadal transients affecting geodetic velocity fields and derived seismicity forecasts in Italy

Michele M. C. Carafa¹✉, Peter Bird², Alessandro Verdecchia³, Matteo Taroni⁴ & Carlo Doglioni^{4,5}

This study critically examines the use of geodetic strain rates for forecasting long-term earthquake rates in a slow-deforming region such as Italy, challenging the prevailing assumption of their temporal stationarity in interseismic stages for seismic hazard analyses. Typically, earthquake-rate models derived from geodesy assume stationary interseismic loading rates, with stress rates in the upper crust proportional to geodetic strain rates, leading to earthquake rates directly proportional to these strain rate tensors. However, our analysis unveils a pronounced correlation between the epicenters of earthquakes that occurred in the past 60–120 years and areas forecasted for higher future earthquake rates based on geodetic strain rates. This correlation appears weak and scattered in analyses of even older earthquakes. To corroborate our findings, we select the 2009 L'Aquila earthquake ($m_w = 6.3$) to prove that its apparently marginal viscoelastic relaxation significantly alters the time series of adjacent benchmarks for the following ~30–60 years, explaining the high correlation between recent earthquakes and strain rate peaks. Our findings require a methodological shift in interpreting geodetic data for earthquake forecasting, emphasizing the two-component (plate-tectonics-driven stationary long-term deformation, and decadal transient viscoelastic relaxation after an earthquake) nature of crustal stress accumulation recorded in geodetic data. We underscore the potential of geodesy-derived forecasts to provide deeper insights into seismic hazards, stressing the importance of acknowledging the long-term temporal variability inherent in geodetic measurements.

Geodetic measurement of crustal strain rates is an essential contributor to long-term seismicity models, because it can detect the accumulation of elastic strain energy even where traditional signs of seismicity are lacking (e.g., where active faults are poorly exposed, or when the historic earthquake catalog is short). Recent models have utilized geodetic data to forecast seismicity, relying on the premise of stationary geodetic velocities between major seismic events. A non-exhaustive list of this rapidly expanding literature goes back to Bird and Liu¹ and Shen et al.². Both models assumed the geodetic velocities to be steady between large earthquakes; Bird and Liu¹ corrected them for near-fault elastic transients and then used them as kinematic constraints for the long-term deformation model, which was then converted into seismicity rate forecasts. Instead, Shen et al.² assumed the amplitude of the earthquake magnitude distribution to be proportional to the maximum horizontal shear strain rate. Then, Bird et al.³ and Bird and Kreemer⁴ converted the Global Strain Rate Map⁵ into a global seismicity rate forecast (but this time, not correcting for near-fault elastic transients). Notably, a global seismicity model including the strain rate contribution⁶ demonstrated good performance both in global and regional perspective experiments^{7,8}.

More recently, regional forecasts have been published for Italy⁹, the India-Eurasia collision zone^{10,11}, the southeastern Tibetan Plateau¹², Japan¹³, and New Zealand¹⁴. Comparing these works, some small differences in

¹Istituto Nazionale di Geofisica e Vulcanologia, L'Aquila, Italy. ²Department of Earth, Planetary, and Space Sciences, University of California, Los Angeles, USA. ³Institute of Geology, Mineralogy, and Geophysics, Ruhr-University Bochum, Bochum, Germany. ⁴Istituto Nazionale di Geofisica e Vulcanologia, Rome, Italy. ⁵Dipartimento Scienze Della Terra, Sapienza University, Rome, Italy. ✉email: michele.carafa@ingv.it

the 2D (or even 3D) strain rate tensors may derive from different schemes for obtaining them by spatial interpolation of the benchmark velocities. Indeed, quantification of geodetic strain rate uncertainties related to data noise and station spacing has been increasingly explored as well as differences in resulting strain rates between methods¹⁵. Using multiple methods to tune parameters and calculate strain rates provides a better understanding of the range of acceptable models for a given velocity field.

Regardless of the numerical differentiation used for interpolating spaced data, the earthquake forecasts assume that the observed velocity field provides a smoother and more stationary representation of seismic potential than the inherently discontinuous record of long-term strain accumulation observed along active faults. However, geodetic strain rates are far from being stationary. Different processes are recorded in time series, such as phase/range errors, periodic signals in site response/multipathing, nontectonic processes (site instability, anthropogenic water withdrawal, recharge, or disposal), glacial isostatic adjustment, stage of the seismic cycle (coseismic, post-seismic or early interseismic, late interseismic) and secular drift. This last process is the main target of neotectonic modelers because it can be reasonably assumed to be constant for thousands of years, and it varies spatially according to the tectonic tractions and the lithosphere strength controlled by frictional slip at low temperatures and dislocation-creep at high temperatures^{16,17}. The assumption of stationarity required for long-term seismicity forecast is valid only if the secular drift is correctly mapped and the other processes are handled correctly.

This work focuses on the latter two processes (stage of the seismic cycle and secular drift) and inspects whether the long-lasting viscoelastic response to an earthquake is incorrectly mapped into (interpreted as) secular drift. If there are no such complications, long-term average strain rates are expected to produce long-term earthquake catalogs as long as the coupled thickness (long-term seismic coupling times the depth extent of seismicity) is correctly defined¹⁸.

Identifying and eliminating the time-variable component due to the seismic cycle is straightforward for the coseismic and early interseismic (postseismic) phases because the process is evident in individual benchmark time series and can be easily subtracted to determine the secular drift; however, after a few years, these effects get smaller and less noticeable, but may still be present and perhaps incorrectly modeled as secular drift. Thus, in this case, geodetic measurements might more accurately be described as the result of a complex interplay between the long-term lithospheric responses to plate tectonic forces, such as brittle-frictional strength at low temperatures and dislocation creep at high temperatures, and the viscoelastic responses of the crust to seismic ruptures that occurred tens of years before and that altered the stress field surrounding the earthquake^{19,20}.

For example, the 1857 Fort Tejon earthquake in California is expected to still perturb the geodetic velocity field, hence the strain rates and the geodetically-derived earthquake rate forecasts. One approach has been recently developed to quantify the viscoelastic perturbations (defined as "ghost transients" in Hearn et al. 2013¹⁹) in the geodetic velocity field of California to correctly calculate steady-state seismicity forecasts. In the original definition, "ghost transients" included but were not limited to postseismic deformation; they are nonzero throughout the whole seismic cycle and define a correction to the velocity field for determining the secular drift and forecasting long-term earthquake rates^{21,22}. Still, discriminating the steady-state long-term contribution from the transient one is tricky because any time-series modeling attempt will remain blind to previous strong earthquakes if their location and magnitude—or even existence—are unknown. Consequently, the principal scientific update of the Western U.S. Geodetic Deformation models was the correction of the geodetic time series to consider the time-dependent relaxation of the lithosphere after a few historic strong earthquakes ($m > 7$). Future deformation models are recommended to include "ghost transients" due to recent earthquakes²³, though their exact position remains challenging for older earthquakes predating an adequate seismic network.

However, if the historical earthquakes of the past 200–300 years and their positions are well known, we could focus on the early stage of the seismic cycle, and then a different scientific question arises: Can time series and resulting strain rate maps conserve the memory of postseismic stresses due to earthquakes that occurred decades/centuries before geodetic measurements? Answering this point is crucial because the criticism of the steady-state assumption regarding geodetic strain rate maps weakens the scientific background of any seismicity forecast derived from geodetic data. However, the ultimate answer cannot solely derive from the geodetic time series. Even after decades of measurements, they will probably not be abundant and precise enough to completely unravel the complexity of the lithosphere viscoelastic behavior. Consequently, if part of the geodetic deformation results from the transient response of the lower crust (or upper mantle) to the most recent large earthquakes and not long-term tectonic forces, the geodetic strain rates must not be used to forecast long-term seismicity without adequate correction of the benchmark time series.

Geodetic measurements and the catalog of past earthquakes in Italy are suitable datasets for investigating the early decadal interseismic stage due to the long and accurate historical seismic catalog and modest rates of tectonic deformation. Italy is part of the greater Alps-Himalayan orogen, and it is currently deforming at low rates; in the Apennines, the long-term horizontal extension rate is roughly 2–4 mm/yr^{24,25} and horizontal convergence in the Southern Alps is not expected to exceed 1–2 mm/yr^{26,27}. These low rates are ideal for better capturing the long-lasting viscoelastic response of the lower crust and upper mantle to the impulsive stresses produced by moderate earthquakes, which might be lost in fast-deforming orogens or plate boundaries. Second, the Italian catalog of historical earthquakes CPTI15²⁸ is probably the most comprehensive, given its completeness (both in space and time), even to relatively low magnitudes. For example, historical and statistical analyses indicate that the catalog has not missed any earthquake with $m_w \geq 5.9$ since 1780 AD²⁹. Thus, analyses of paleoseismic data and active faults are in the fortunate situation of complementing the numerous historical sources instead of providing loose estimates for the earthquake epicenters (See Fig. 1).

Given these peculiar geodynamic and historical circumstances, our investigation of the spatial and temporal effects of previous earthquakes on geodetic strain rate maps has potentially far-reaching implications for many regions of the Earth, enhancing the methodological framework for correlating strain rate maps to seismicity forecasts and/or the long-term viscoelastic response of the lithosphere to earthquakes.

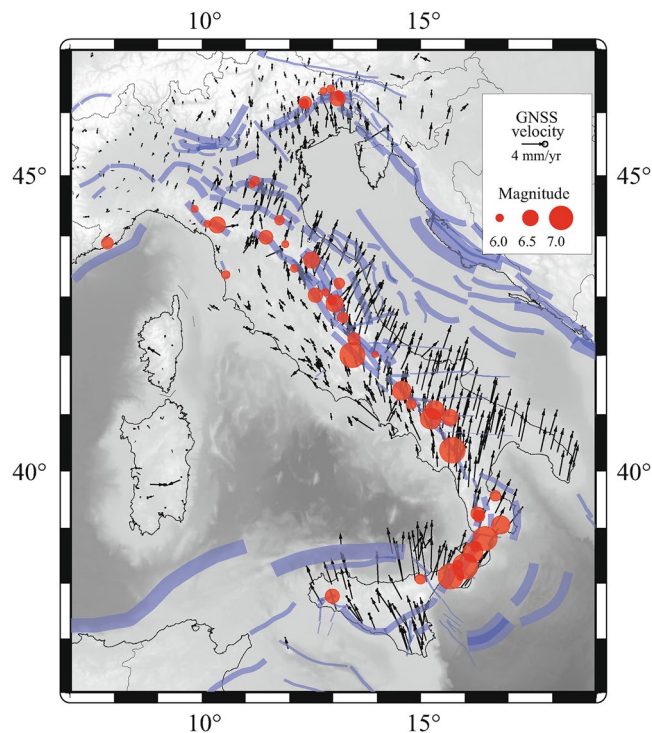


Fig. 1. In red the $m \geq 5.9$ earthquakes from the CPTI15 catalog since 1780 AD, in purple the Seismogenic Sources (active faults) from DISS 3.3.0 database³⁰, in black the geodetic velocities from Serpelloni et al.²⁵, relative to stable Eurasia.

Results

Background to the modeling approach

The classical viscoelastic cycle for a volume of the crust in an active orogen (as the central Mediterranean) is relatively simple: slip along a fault occurs when the shear traction on the fault surface is equal to the frictional threshold, allowing the blocks to slip on the two sides of a fault. As sliding starts, the fault friction decreases. If the decrease is fast enough, it may lead to accelerations in the surrounding crust, which may produce seismic waves. A slower decrease in fault strength may give rise to an aseismic slip event. Whether slip is fast or slow, the analytic theory for dislocation patches in elastic half-spaces shows that deviatoric stresses (if initially quasi-uniform) will decrease in two large volumes adjacent to the rupture surface, while increasing in smaller volumes adjacent to the rupture edges (e.g., King et al.³¹). In the few years after the earthquake, the newly-stressed margins of the rupture and adjacent crustal and upper-mantle volumes respond viscoelastically to these stress changes. In this phase, the strain rates (and the stress rates) for fault-adjacent crustal volumes likely exceed their long-term rates. Note that under this time-dependent scenario, the incremental strain rates and stress rates initiated by fault slip are expected to diminish as the relaxation of transient stresses in the rupture-margin zones is completed. In a later phase, adjacent crustal volumes may experience strain rates lower than the long-term tectonic ones^{19,21}. The duration of the initial phase remains uncertain: postseismic transients, such as the poroelastic rebound or afterslip, are better captured and reported in the first months to years after strong earthquakes. However, increasing literature suggests long-lasting transients, including the spread of viscoelastic relaxation of the lower crust and upper mantle and localized afterslip of the deep shear zones.

To check whether the interseismic geodetic strain rates for the Italian peninsula are stationary, we performed a statistical test comparing the position of past epicenters with the patterns in the earthquake rate forecast maps derived from uncorrected geodetic strain rates. For this aim, we first determined the spatial distribution of the averaged long-term interseismic model of 2D strain rates with NeoKinema code^{1,32}, under the traditional assumption that the geodetic velocities mainly contain the long-term secular drift. The model strain rates have been determined through a joint inversion process, integrating the geodetic velocities from Serpelloni et al.²⁵ and the interpolated SHmax directions from Mariucci and Montone³³, which have been proven to be effective in reducing the noise of non-tectonic transient of geodetic data³⁴. While the authors have removed coseismic and very early postseismic deformations for the strongest earthquakes that occurred in Italy after 2009 in the solution of Serpelloni et al.²⁵, we adopted the scheme reported in Bird and Carafa³² to discount the inflation/deflation of the magma chambers of active volcanoes. Then, we forecasted earthquake rates from geodetic strain rates, assuming a Tapered Gutenberg-Richter earthquake size distribution³⁵ [see Methods]. Forecasts have been determined on an equally-spaced grid of 0.2° ; we staggered the forecast cells, creating 4 variants of the same forecast to better capture the spatial uncertainty of the strain rate estimates due to the cell position (Fig. 2).

The seismicity forecasts derived from geodesy are expected to exhibit a smoother map pattern than those derived from a fault model; despite these differences, integrating the moment rate from a strain rate model or

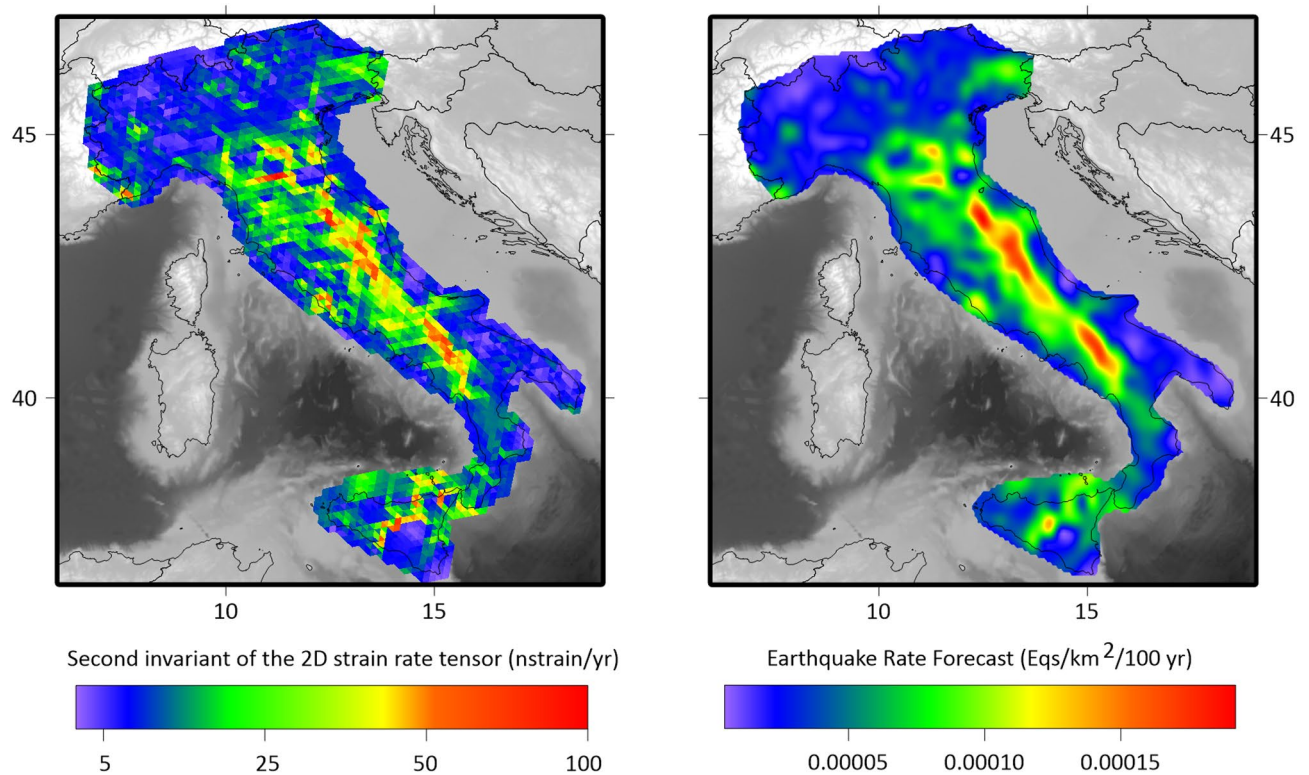


Fig. 2. Left: the reference strain rate model determined with NeoKinema. Right: earthquake rate forecast on a $0.2^\circ \times 0.2^\circ$ grid (see Methods for detail on translating the strain rates into earthquake rates).

a fault model should yield identical results if geodetic strain rates are stationary. Hence, the seismicity model can be scored against actual earthquakes to test its spatial performance and stationarity in time. To measure if and how well past epicenters reported in the historical CPTI15 catalog match the forecast peaks, we applied the information score (success) I_1 ³⁶ which can be described as the mean information gain (measured in binary bits) per earthquake over a simple model with a spatially uniform earthquake rate (see Methods). The lower the I_1 , the worse the model performance in reproducing the spatial pattern of the test earthquake catalog. Basically, our statistical test is a retrospective performance of the earthquake rate forecasts and the strain rate map and simultaneously checks whether the pattern of the I_1 variation is informative of the stationarity of stressing rate on the crustal volumes after strong earthquakes in Italy. The underlying idea of this test is that I_1 may be randomly distributed around its central value if the strain rate map were free from any transient viscoelastic strain rates (due to the early interseismic stage) and genuinely representative of long-term deformation rates; otherwise, an increasing pattern of I_1 moving to the present should be evident.

After some preliminary examinations, we chose $m \geq 5.9$ as the minimum magnitude for defining the test earthquakes. However, our results remain valid for higher magnitudes; this threshold allows us to consider a consistent number of historical earthquakes since 1780 AD, which approximately defines the completeness year for $m \geq 5.9$. We also examined the impact of CPTI15 earthquake epicenter errors, which were reported to vary up to 8–10 km, by generating perturbed catalogs based on the 1-sigma uncertainty. Randomly sampling these errors, we assessed their effect on the I_1 standard deviation across ten synthetic catalogs and found it remained stable irrespective of grid spacing [see Methods].

I_1 peaks: distinguishing active faults from stable regions?

The analysis of spatially-staggered grid forecasts for the 47 $m \geq 5.9$ earthquakes from the CPTI15 catalog reveals I_1 scores ranging between 0.59 and 0.78. This means that the grid cells containing these earthquakes generate seismicity forecasts, and describe 2D strain rate tensors, which are 50% to 75% higher than the average across Italy. The I_1 scores for $m \geq 5.9$ earthquakes prompt two possible interpretations: (a) the spatial peaks in strain rate reflect the secular drift, hence they are stable, long-term indicators of regions with a higher seismicity forecast, as validated by historical earthquake epicenters, or (b) the strain rate peaks are influenced by the ongoing response of the lithosphere to recent seismic events, hence not fully representative of the secular drift (Fig. 2).

We tested the first option using Italian active faults (seismogenic sources from the DISS database, DISS 2021). Although Italy is in a slow-deforming sector of the Alpine-Himalayan orogen³⁷ without distinct plate boundaries, earthquakes are predominantly concentrated along active faults of the Apennines and the Southern Alps (see Fig. 1). The distribution of historical earthquakes might suggest that the I_1 pattern reflects an average scenario where earthquakes randomly occur on active faults. The I_1 scores of the $m \geq 5.9$ CPTI earthquakes and DISS active faults (seismogenic sources) should be comparable in this case. To explore this scenario, we assessed I_1 values based on the surface projections of seismogenic sources from the DISS database against earthquake

forecasts derived from strain rate maps. We are aware that a fraction of differences in seismicity forecasts among various active faults could be attributed to varying slip rates. However, a meta-analysis on throw rates by Carafa et al.³⁸ revealed that conventional sampling techniques often underreport slip rate uncertainties, a discrepancy highlighted when multiple methodologies assess the same fault. Given the overlap between the uncertainty of slip rates and the slip rates themselves (~ 0.5 mm/year) for the Italian territory, we built a synthetic long-term earthquake catalog uniformly sampling the surface projection of DISS seismogenic sources (DISS Working Group, 2021³⁰; see Method). The calculated I_1 from the DISS-derived seismicity catalog, juxtaposed with geodesy-derived forecasts, yielded a gain of $I_1 \approx 0.15$, indicating the DISS seismogenic sources describe strain rate regions with slightly higher strain rate than the Italian average but lower than that $0.59 \leq I_1 \leq 0.78$ of recent earthquakes. The two I_1 are not comparable, and this discrepancy steers us towards the latter interpretation, suggesting a temporal pattern in geodetic strain rates with their peaks linked to the time elapsed since the most recent seismic events. At this point, we hypothesize that this temporal pattern is likely due to the lithosphere volumes being in an early interseismic stage, thus deforming at a higher rate than expected for secular drift. In Fig. 3, we chart the year against I_1 for each analyzed earthquake, the average I_1 for $m \geq 5.9$ CPTI earthquakes, and the I_1 for the DISS-derived earthquake catalog, which appears to define a rough minimum for I_1 of earthquakes since 1780. This pattern indirectly supports the hypothesis that plate-tectonic long-term and short-term stresses from recent earthquakes sum up and drive the lithospheric viscoelastic response. Furthermore, the low I_1 of Italian active faults seems to confirm that in slow-deforming orogen, it is hard to capture the interseismic stage of active faults if they are not known in advance.

I_1 peaks: testing the time-dependent gain influenced by recent earthquakes

Once we had collected these indications that the observed strain rate pattern (and the associated seismicity forecast) was a complex viscoelastic response of the lithosphere characterized by multiple decay times, we performed some tests to reinforce (or refute) our findings.

First, we note that the GNSS solution used to derive the earthquake rates already contains an exponential adjustment of the GNSS time series calibrated to the first few months after the earthquake occurrence. However, this correction may not capture multiple decay times, thus the comprehensive viscoelastic deformation spectrum. Furthermore, observed strain rate peaks may stem from earthquakes preceding the GNSS measurement period, which are not included in the time series correction.

To better enlighten the time variability of I_1 , we analyzed the contribution to each $m \geq 5.9$ earthquake since 1780 (Fig. 3), which reveals a trend where the contribution to the gain increases closer to the present day. Further emphasizing this point, we computed the moving average of I_1 for sets of 10 events (adjacent in time) based on the 47 $m \geq 5.9$ earthquakes recorded over the past 240 years. This analysis identified the highest moving average of $I_1 = 1.37$ for the most recent 10 earthquakes, from the 1976 Friuli earthquake to the 2016 Norcia earthquake. This finding indicates that grid cells encompassing the latest 10 $m \geq 5.9$ earthquakes exhibit an increase of 2.6 in the strain rate than the overall spatial average. Over time, the observed rising trend of I_1 points to multi-decadal, time-dependent transients following historical seismic events, as well as a component of long-term steady-state tectonic loading.

We conducted a further statistical analysis to determine when the I_1 gain becomes negligible, dividing the catalog of 47 magnitude ≥ 5.9 earthquakes into two temporally-separated groups. The initial set comprises older earthquakes, while the latter consists of recent events. By shifting the central year, which separates the two subsets, and applying a Wilcoxon test, we identified significant I_1 median differences between the groups (Fig. 4). According to this test, the period from 1900 to 1960 AD marks the divide, segregating the catalogs into an older segment with lower I_1 and a newer one with greater I_1 , indicating that the duration of the long-lasting postseismic transient approximates 60–120 years. This conclusion aligns with the I_1 temporal trend (Fig. 4).

Our Methods section validates that our results remain unaffected by specific interpolation parameters or grid cell spacing choices. In detail, any interpolation with an L_2 -norm to geodetic data within 0.3 to 0.7 mm/year and grid spacing for seismicity forecasts in the 0.1° – 0.3° range consistently demonstrates the same I_1 enhancement for post-1900 AD earthquakes.

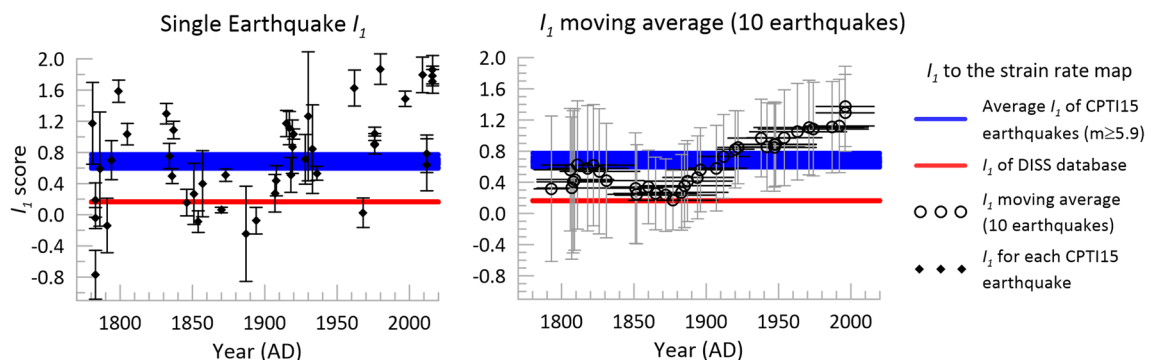


Fig. 3. I_1 score for each single earthquake in the CPTI15 historical catalog and I_1 moving averages determined on 10 earthquakes (adjacent in time). The average I_1 of CPTI15 and DISS are reported.

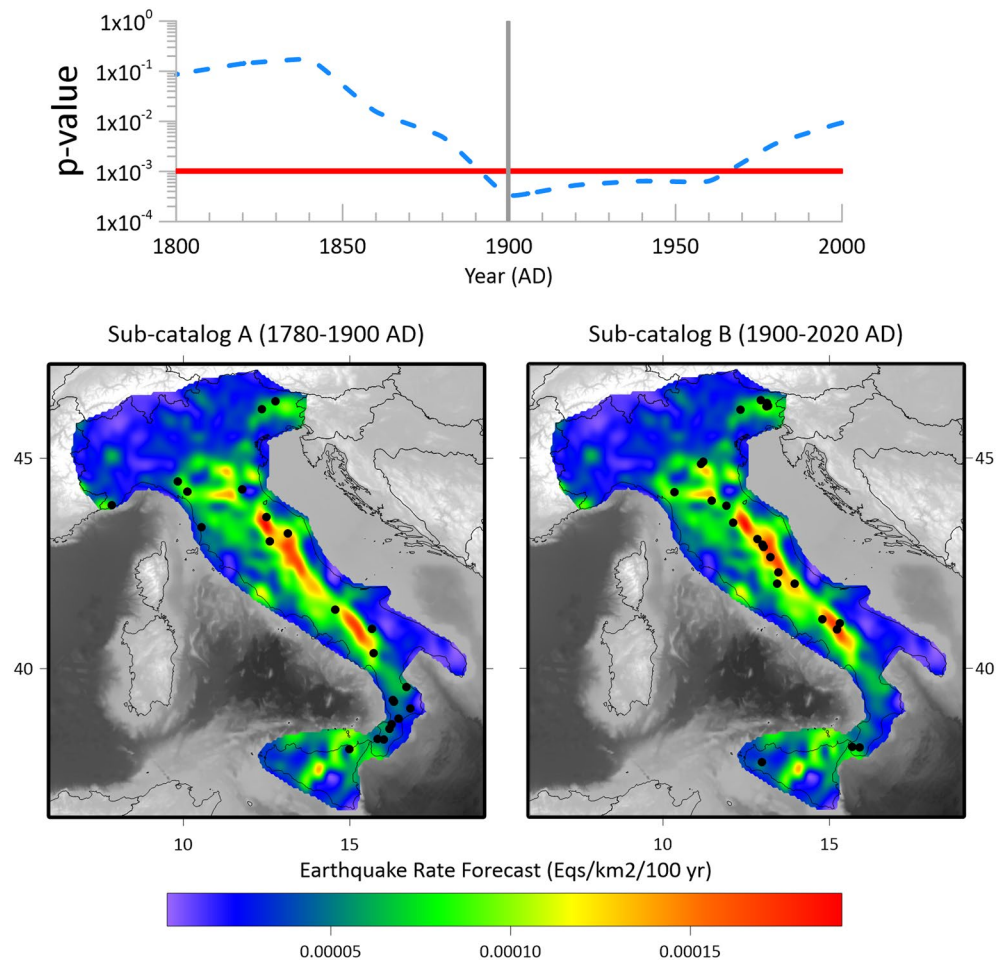


Fig. 4. Statistical test to discriminate the year dividing older earthquakes with random and lower I_f from recent ones with higher I_f . The p -values are reported with the dashed blue line. The p -value below the red line (p -value = 0.001) identify the years for which the two catalogs are statistically different. The minimum p -values are found in the range 1900–1960 AD. Hence, the earthquake population before 1900 AD is significantly different than the one after 1960 AD, with the transition between the two being unclear. In the map, we plot the two sub-catalogs that resulted from the lowest p -value in 1900 AD (grey vertical bar).

A case study: the multi-decadal transient due to the L'Aquila 2009 ($m_w=6.3$) viscoelastic relaxation

To elucidate the long-term effects of a moderate earthquake on the geodetic strain rate map of a slow-deforming orogen such as the Alps-Apennines, we selected the 2009 L'Aquila earthquake. Previous literature has predominantly focused on afterslip distribution, released mainly within the first 300 days post-earthquake^{39,40}. These studies explicitly overlooked the longer-term viscoelastic relaxation due to the short duration of the investigation periods^{40,41}. To fully assess the subtle yet enduring viscoelastic relaxation and to discount the influence of residual afterslip—which predominantly affected benchmarks near the causative fault—we selected only stations positioned longitudinally to the fault strike and located more than 40 km from the fault. This choice resulted in 14 well-placed benchmarks to capture potential transients (see Fig. 5). We analyzed two interseismic solutions: the first ended on the day of the main event (6th April 2009), and the second spanned from 1st June 2010 to 24th August 2016, ending with the $m_w=6.1$ Amatrice earthquake, which likely influenced the viscoelastic response initiated by the L'Aquila earthquake.

We tested various rheologies to match the observed differences in velocity solutions before and after the L'Aquila event to the predicted viscoelastic responses of the lithosphere. Several viscosity profiles were found to better explain these differences through a viscoelastic transient rather than through measurement random noise (see Methods for details). Based on the geodynamics of the area, we selected as the preferred viscoelastic model for the Tyrrhenian benchmarks the one with a lower crust analogous to a Maxwell body (viscosity = 5×10^{18} Pa-s) and an upper mantle resembling a Burger body, characterized by short-term viscosity of 5×10^{17} Pa-s and long-term viscosity of 1×10^{19} Pa-s. Conversely, the Adriatic lithosphere is modeled similarly for the lower crust but with a stronger upper mantle (short-term viscosity of 5×10^{17} Pa-s and long-term viscosity of 1×10^{21} Pa-s), reflecting the geodynamic settings of the Adria foreland^{42–44} (see Methods). The elastic parameters for both

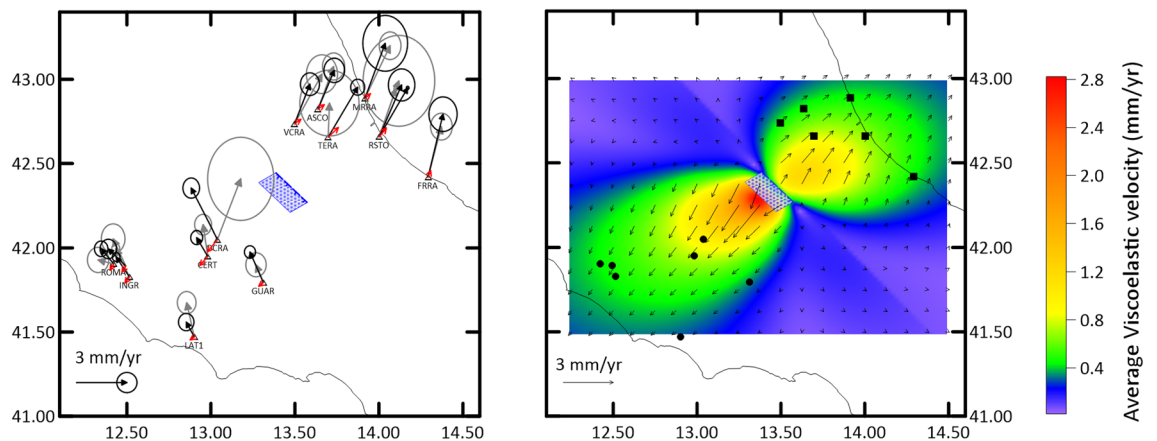


Fig. 5. Left: horizontal velocities before (in grey) and after (in black) the 2009 $m_w=6.3$ L'Aquila earthquake. The causative fault (in blue) and coseismic and early postseismic are from Ragon et al.⁴⁸. The modeled horizontal average velocities of the viscoelastic transient are plotted in red. Right: the spatial distribution of intensity and direction of the viscoelastic transient between the 1st of June 2010 and the 24th of August 2016. Black squares represent the Adriatic benchmarks, and black circles represent the Tyrrhenian benchmarks (Color figure online).

the Tyrrhenian and Adriatic lithospheres were derived from seismic velocities and densities as determined by Magnoni et al.⁴⁵. The improvement of this model over a model attributing differences to measurement errors is above 25% for the Tyrrhenian side and approximately 20% for the Adriatic side.

The viscoelastic velocities in this model exhibit temporal and spatial trends that mirror the long-term interseismic extensional strain rate (secular drift) expected for the central Apennines. This compatibility between the secular drift and the early interseismic phase implies a non-marginal possibility of overlooking the transient signal due to the viscoelastic relaxation. If we consider two points located longitudinally from the fault strike on both hangingwall and footwall to a distance of 50 km, this transient extension rate peaks in the first decade after the earthquake, averaging approximately 0.6 mm/yr, and may remain greater than 0.3 mm/yr for the following 30 years, persisting above 0.15 mm/yr for approximately 50–60 years. These findings are unaffected by the subjective choice of viscosities, as detailed in the Methods section, and align with: (a) the 60-to-100-year interval in which the elapsed time of earthquakes still shows a consistent I_1 gain in the strain rate map; (b) the Wilcoxon test for splitting the earthquake catalog into two statistically distinct sets with different I_1 gains. This case study suggests that the postseismic effects of similar earthquakes (e.g., the 1997–1998 Colfiorito earthquake) or even larger ones (e.g., the 1980 Irpinia earthquake) from the past 60–100 years continue to influence time series data, potentially amplifying the long-term secular drift.

Although these rates might seem minor along fast-deforming plate boundaries, they are significant to the long-term interseismic strain rates in a slowly deforming region like Italy. Notably, the subtle impact of the postseismic viscoelastic transient from the L'Aquila earthquake is evident when comparing interseismic strain rates calculated with geodetic data gathered and published before the earthquake—or explicitly excluding any data thereafter^{46,47}—with more recent measurements that include a decade post-event, encapsulating the viscoelastic response.

Discussion

Transient rheology and its implications for seismic hazard assessment

The main target of our work was to understand whether the peaks in the strain rate map of a slow-deforming region, such as the Alps and Apennines, were genuinely representative of the secular drift or partially related to the subtle multi-decadal transients of recent earthquakes. Our analysis, spanning 240 years of complete earthquake catalog for magnitude $m \geq 5.9$ and investigating the effect on long-term interseismic transient due to the viscoelastic relaxation after the L'Aquila 2009 earthquake, has revealed that geodetic strain rate maps of Italy highlight crustal volumes with transient viscoelastic relaxation and thus with overpredicted future earthquake rate densities. This unrealistic pattern of the steady secular drift, resulting from transient responses to earthquakes over the past century, challenges long-held assumptions in the seismic hazard community about the stationarity of geodetic strain rates for earthquake rate calculations. Such findings resonate with existing literature, including Ingleby and Wright⁴⁹, suggesting postseismic transient patterns may persist for decades, possibly necessitating a new evaluation of seismic hazard models to account for these processes. In this sense, there is an apparent misalignment (or an incomplete knowledge transfer) between the seismic hazard community and the geodetic communities because the former has not yet entirely accepted the information that geodetic strain rates are not stationary. In contrast, the geodetic community is almost unequivocal on this point because many works have argued for long-term non-steady deformation by investigating the long-term effects of the viscoelastic response to past earthquakes^{50–52}.

Two competing (and possibly complementary) models can explain the transient spatial pattern of recent earthquakes: deep fault shear zone deformation in 2-D or viscoelastic relaxation of the crust and mantle in

3-D. The main difference between the two models is the localized spatial pattern of a few tens of kilometers around the fault for the first hypothesis, which agrees with geological findings from exhumed roots of faults showing that deformation at depth is delimited into shear zones up to a few kilometers wide^{53–56}. A broader and smoother deformation pattern characterizes the viscoelastic relaxation of the lithosphere. In the case of the L'Aquila earthquake, we have proved that the viscoelastic transient can explain the different velocities before and after the earthquake. Still, we think our analysis is inadequate in discriminating among complementary processes, underscoring the complexity of interpreting geodetic data to accurately model the time-varying spatial patterns of each postseismic process. For example, different works^{57–59} reported an apparent increase in the lower crust and upper mantle viscosity over time after earthquakes, whereas other works have reported possible smaller viscosities for the lithosphere closer to the earthquake than for the distant one⁶⁰. A complicating factor is that if relaxation is governed by nonlinear dislocation creep, then effective viscosity is not a simple material property but also depends on the differential stress level. This point may explain viscosities that appear to change through time. Thus, it cannot be excluded that late transients after an earthquake localize in the surrounding of the host-fault due to viscosity variation of the deep shear zone, which we excluded in our modeling of the lithosphere viscoelastic transient due to the L'Aquila earthquake.

Seismic hazard: future directions and stakeholder engagement

In past years, the catalog of historical earthquakes has been the primary input for seismic hazard models in Italy, with the geological information being supplementary to provide some kinematic constraints. An ensemble model of ten seismicity forecast rates has been calculated in the recently published Italian Seismic Hazard Model²⁹. The summed weight of the seven forecasts based primarily on the historical catalog is 0.85, whereas a weight of 0.13 was assigned to the forecast mainly based on the database of the seismogenic sources (*i.e.*, faults; DISS Working Group, 2021³⁰). The remaining marginal weight (0.02) given to the two geodetic models describes an open-minded but cautious approach toward the geodetic measurements in a region with a well-populated historical catalog (likely the richest of sources describing the earthquake effects in historical times) and a well-rooted experience with fault-based seismicity rates forecasts. Instead, the two geodetically-derived earthquake forecasts resulted from recent modeling^{9,26,61} on converting geodetic strain rates to earthquake forecasts under the assumption of steady state interseismic horizontal velocities at GNSS benchmarks. In this sense, our results support the cautious choice of small weight assigned to the geodetic-derived seismicity forecasts for a national seismic hazard to be used for emergency planning and seismic risk mitigation.

Our study underscores the opportunity to improve geodesy-derived seismic forecasts, advocating for time series corrections informed by independent physics-based models as we proved for the multi-decadal viscoelastic transients of earthquakes. Geodetic solutions need to be adjusted to meet the requirements demanded by long-term seismicity forecast models, which assume long-term steady rates. However, this assumption is not universally valid in Italy, as we have proved that time-dependent multi-decadal lithosphere viscoelastic responses to moderate-to-strong earthquakes can occur. Additionally, geodesy-based forecasts assume that the stress rates in the upper crust are proportional to the geodetic strain rates, which is false in some regions undergoing distributed permanent deformation or along faults with aseismic sliding. Thus, it is rational and important for catalog-based forecasting to check and supplement geodesy-based forecasting.

Furthermore, while short-term transients like hydrological changes or slow landslides are typically handled through the use of independent datasets, our work challenges the assumption popular in the seismic hazard community that the resulting interseismic velocities are truly stationary over decades to centuries. The geodetic community is almost unequivocal in rejecting this assumption because many works have argued for long-term non-steady deformation by investigating the long-term effects of the viscoelastic response to past earthquakes.

This point highlights the necessity for a complete knowledge transfer between the geodetic and seismic hazard communities to establish advanced methodologies that accurately capture the complexities of time-dependent crustal deformation over prolonged periods and, consequently, determine robust seismicity forecasts. Accordingly, in slow-deforming regions affected by moderate earthquakes, increasing the density of benchmarks in areas impacted by historical earthquakes could provide finer resolution data to better characterize changes in lithospheric viscosity over time and better seismicity forecasts.

Future research should leverage high-resolution geodetic measurements (both GNSS and InSAR) and interdisciplinary approaches between geodesy analysts, neotectonic and seismic hazard modelers to develop more accurate and effective discrimination between the secular drift and the transient correction due to the stage of the seismic cycle for any volume of the lithosphere. We anticipate that progress in these areas will lead to greater collaboration with stakeholders such as policymakers, urban planners, and the insurance industry, which is essential for turning these scientific discoveries into practical measures for mitigating seismic risks.

Method

Interseismic strain rate model and Seismic Moment Rate

The spatial distribution of long-term-average interseismic 2D surface strain rates is calculated with NeoKinema^{1,32}, a code validated across various orogens^{62–64} and applied in the calculations of earthquake rate distributions⁶⁵. The model strain rates are determined through a simultaneous inversion process, integrating the interseismic geodetic velocities from Serpelloni et al.²⁵ and the interpolated SHmax directions from Mariucci and Montone³³, which reduce the noise of non-tectonic transient in geodetic data²⁶. SHmax interpolation across the study area is performed according to the methodology developed by Carafa & Barba⁶⁶ and Carafa et al.⁶⁷, which builds upon the foundational work of Bird & Li⁶⁸. However, in this version of NeoKinema modeling no fault traces or geologic estimates of fault offset-rates were used.

The general objective function of NeoKinema, which is maximized, is:

$$\Pi \equiv -(\vec{p} - \vec{r})^T [\tilde{C}_{\text{GPS}}^{-1}] (\vec{p} - \vec{r}) - \frac{1}{A_0} \sum_{n=1}^3 \iint_{\text{area}} \frac{(p_n - r_n)^2}{\sigma_n^2} da \quad (1)$$

where \vec{p} is the vector of (scalar) model predictions, and \vec{r} is the vector of (scalar) data; \tilde{C}_{GPS} is the long-term covariance matrix and $n = 1, 2, 3$ enumerates 3 target rates associated with 3 independent functionals of permanent strain-rate at each continuum point. In detail, $n = 1$ is the continuum stiffness to be set under the microplate constraint; $n = 2$ is the isotropy constraint that allows the 2D strain rate tensor to be oriented as the stress tensor and $n = 3$ (not necessary everywhere) is a constraint on the relative size of the principal strain rate values to match the sense of interpolated regional stresses.

The long-term covariance matrix \tilde{C}_{GPS} is built following the approach of Bird and Carafa (2016); the geodesy-derived earthquake rate relies on the assumption that the secular drift at each GNSS benchmark describes the long-term stationary velocity field. Consequently, any further processes stored in the time series (site instability; anthropogenic water withdrawal, recharge, or disposal; hydrocarbon extraction; magma chamber inflation or deflation; glacial isostatic adjustment; velocity change due to stress perturbation from the coseismic and early interseismic stages of the seismic cycle) have to be modeled as noise sources obscuring the secular drift. If a simple physical model can describe one of these processes, then the \tilde{C}_{GPS} is augmented by the transpose products of the corresponding velocity perturbation vectors. Carafa and Bird²⁶ have proved this approach to be adequate to isolate the secular drift, and we applied a similar approach to the dataset of Serpelloni et al.²⁵. In the case of this velocity solution, the time series have already been corrected for the velocity changes due to coseismic and afterslip (but not for those due to viscoelastic relaxation). Thus, we built the \tilde{C}_{GPS} by using the geodetic uncertainties and then augmented it with inflation/deflation of magma chambers reported in Carafa and Bird²⁶ by modeling them as Mogi sources.

Once we have defined the \tilde{C}_{GPS} , we endeavor to optimize the critical parameter A_0 in Eq. (1) to obtain stable results regarding spatial strain rate peaks and past earthquake positions. Essentially, a higher A_0 value favors precise geodetic data fitting, reducing the focus on continuum stiffness and stress direction constraints. On the other hand, a lower A_0 value implies a readiness to compromise GPS data fitting in favor of a smoother solution that minimizes permanent strain-rates between faults and incorporates stress directions where they exist.

To present our results, we selected $A_0 = 23 \times 10^7 \text{ m}^2$ as the exemplary model due to its balanced compromise between geodetic fitting and stress data integration. Specifically, the L_2 -norm misfit between geodetic observations and predictions is 0.45 mm/yr. Nonetheless, we examined five different models to assess the impact of A_0 smoothing on the strain rate map and past earthquake positions. These models and their L_2 -norm relative to horizontal geodetic measurements in Italy are detailed in Table 1, with their corresponding strain rate maps illustrated in Fig. 6.

Earthquake forecast from a 2D horizontal strain rate tensor

Let's define $\dot{\epsilon}_{1h}$ and $\dot{\epsilon}_{2h}$ as the principal values of the 2D horizontal strain rate tensor (approximated by the geodetic strain rate tensor) in a region, with the long-term vertical strain rate defined as $\dot{\epsilon}_{rr} = -(\dot{\epsilon}_{1h} + \dot{\epsilon}_{2h})$ for permanent strain mechanisms that conserve volume. To convert the interseismic strain rate into a seismicity rate forecast, we first calculated the seismic moment rate as

$$\dot{M}_s = \langle cz \rangle \cdot \mu \cdot A \cdot \left(\frac{\dot{\epsilon}_{mid}}{\cos(\theta_1) \cdot \sin(\theta_1)} + \frac{\dot{\epsilon}_{least}}{\cos(\theta_2) \cdot \sin(\theta_2)} \right) \quad (2)$$

where μ is the elastic shear modulus, A is the surface of the investigated area, $\langle cz \rangle$ the average coupled thickness (c is the seismic coupling and z the seismicity cutoff depth roughly corresponding with the transition between the brittle/frictional upper crust and the viscous/ductile lower crust), $\theta_1 = \theta_2 = 30^\circ$ is the angle between the two active fault populations and the principal strain rates $\dot{\epsilon}_{mid}$ and $\dot{\epsilon}_{least}$, which are defined as $\dot{\epsilon}_{mid} = \dot{\epsilon}_{great} - \dot{\epsilon}_{least}$ with $\dot{\epsilon}_{great} = \sup(|\dot{\epsilon}_{1h}|, |\dot{\epsilon}_{2h}|, |\dot{\epsilon}_{rr}|)$ and $\dot{\epsilon}_{least} = \inf(|\dot{\epsilon}_{1h}|, |\dot{\epsilon}_{2h}|, |\dot{\epsilon}_{rr}|)$. The most subtle and unknown parameter is $\langle cz \rangle$, which is often overlooked under the strong assumption of total seismic coupling leading to $\langle c \rangle = 1$. In the absence of evidence about its value, the most straightforward approach to get around the $\langle cz \rangle$ calculation is to assume that \dot{M}_s follows a Tapered Gutenberg-Richter distribution³⁵, and can be explicated as

A_0 ($\times 10^7 \text{ m}^2$)	L_2 -norm (mm/yr)
5	0.72
15	0.50
23	0.45
40	0.40
55	0.30

Table 1. Selected NeoKinema models and their L2-norm misfit to geodetic data.

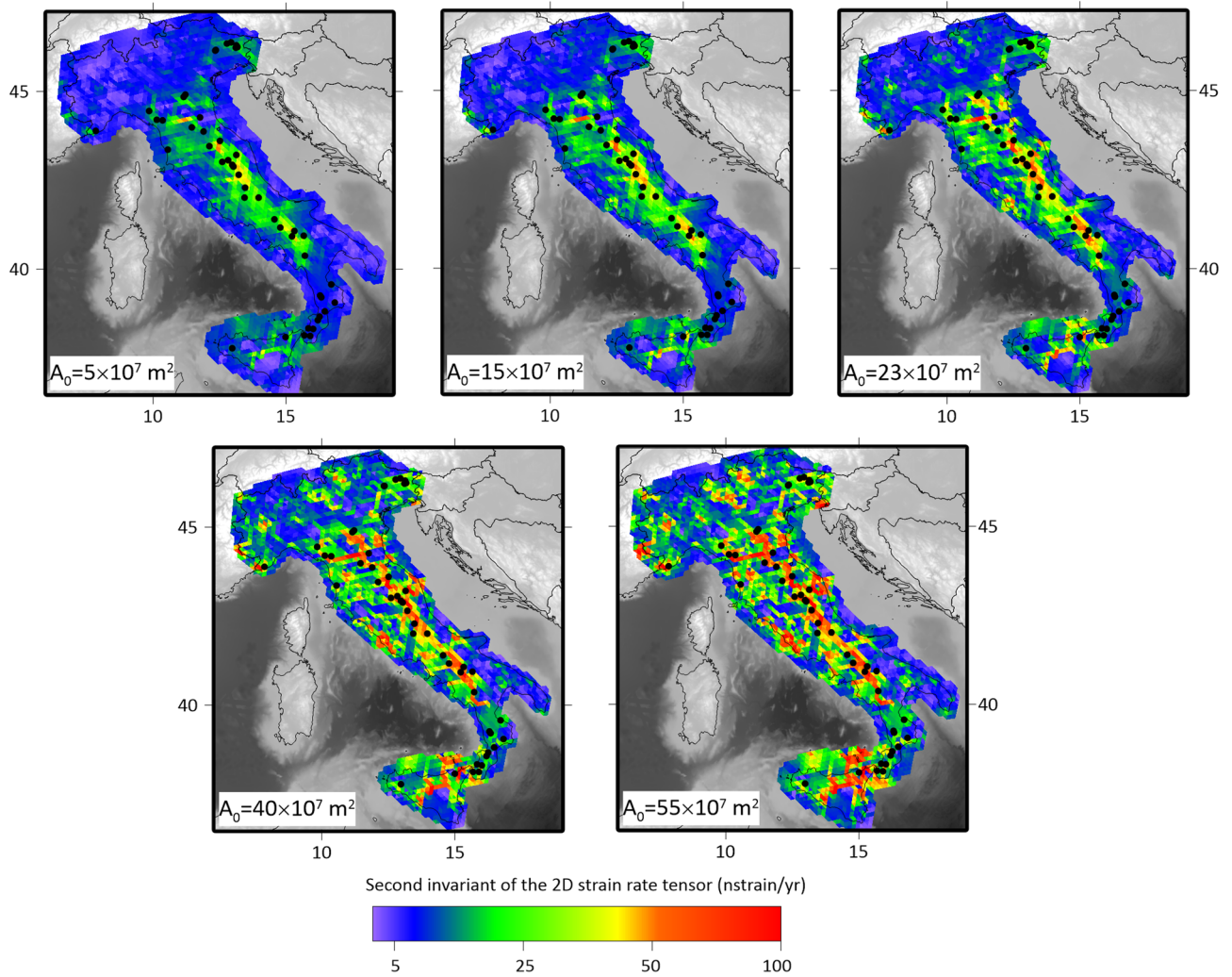


Fig. 6. Five alternative strain rate maps using different A_0 parameters. The strain rate map with $A_0 = 23 \times 10^7 \text{ m}^2$ is the reference model for our calculations, although our results are also valid for the other four models.

$$\dot{M}_s = \frac{\alpha_0 \cdot M_t^\beta \cdot \Gamma(2 - \beta)}{1 - \beta} \cdot M_c^{1-\beta} \cdot \exp\left(\frac{M_t}{M_c}\right) \tag{3}$$

where α_0 is the number of earthquakes above the threshold seismic moment M_t in the investigated period, Γ is the gamma function, M_c the corner seismic moment, β the asymptotic spectral slope at small moments. It follows that

$$\langle cz \rangle = \frac{\frac{\alpha_0 \cdot M_t^\beta \cdot \Gamma(2-\beta)}{1-\beta} \cdot M_c^{1-\beta} \cdot \exp\left(\frac{M_t}{M_c}\right)}{\mu \cdot A \cdot \left(\frac{\dot{\epsilon}_{mid}}{\cos(\theta_1) \cdot \sin(\theta_1)} + \frac{\dot{\epsilon}_{least}}{\cos(\theta_2) \cdot \sin(\theta_2)} \right)} \tag{4}$$

By setting Eq. (2) and Eq. (3) equal to each other, we can compute earthquake rates (for various magnitudes) from strain rates, with an overall calibration to historic seismicity rates. Our brief term for such a product is a "seismicity forecast." Here, "seismicity" means the rate of earthquake epicentroids, per unit of map area, above a pre-defined threshold magnitude. While a "forecast" is normally intended to apply to new earthquakes occurring after the date of forecast computation and publication, it can also be scientifically interesting to compare such "forecasts" retrospectively to existing earthquake catalogs.

For Italy, we used the CPTI15 (version 4.0, Rovida et al., 2020) catalog of historical earthquakes to determine M_t , M_c and β and, consequently, to calculate \dot{M}_s in Eq. 3 (see Table 2 and Fig. 7). Then, we used these values and the strain rates from each deformation model with variable A_0 to determine the coupled thickness (cz) as in Eq. (4). In this way, the total seismic moment is set to \dot{M}_s for all deformation models, but its spatial distribution follows the strain rate pattern which differs for each deformation model (see Fig. 6).

The threshold magnitude m_t and its changes through space and time are defined both with historical and statistical approaches²⁹. Using the m_t thresholds, we applied the Kijko and Sellevoll⁶⁹ approach, modified for the

m_i	4.5
m_c	7.2
β	0.70
$\alpha_0(\text{eqs yr}^{-1})$	5.27

Table 2. Tapered Gutenberg-Richter parameters for converting the strain rate tensor in seismicity forecasts.

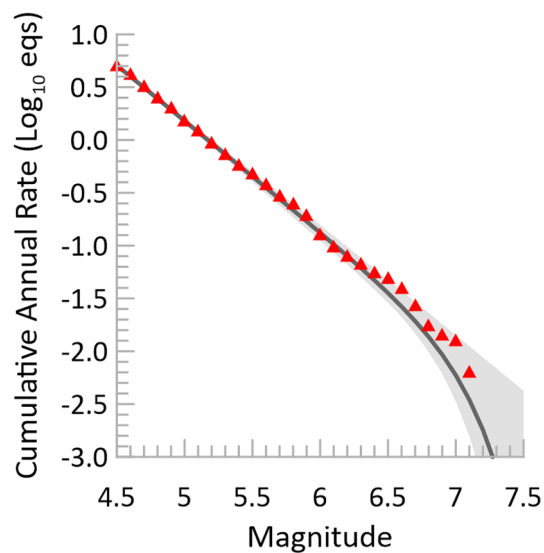


Fig. 7. Parameters of the Tapered Gutenberg-Richter determined from CPTI15 catalog²⁸. The cumulative number of observed earthquakes is plotted as a red triangle for each magnitude bin. The modeled earthquake distribution is represented with a black continuous line. The grey area represents the confidence interval of the model.

tapered Gutenberg-Richter distribution⁷⁰, to estimate with the maximum likelihood method the parameters M_c and β .

Finally, the earthquake rate forecasts are calculated on a grid of $0.2^\circ \times 0.2^\circ$; we staggered the forecast cells, creating 4 variants of the same forecast to better capture the spatial uncertainty of the strain rate estimates due to the cell position.

Information score I_1 and used catalogs (CPTI15 and DISS)

Once we built the seismicity forecasts, we focused on two catalogs to compare them to the forecasts. The first comprises the 47 $m \geq 5.9$ historical earthquakes reported in CPTI since 1780 AD (see Fig. 8), which roughly corresponds to the completeness year for this magnitude²⁹. We chose this specific magnitude threshold to ensure a sufficient sample size of earthquakes for observing any potential variations in the stress rates of crustal volumes between two moderate-to-strong earthquakes, particularly in regions characterized by slow deformation, such as the Alps and Apennines.

The second is a synthetic earthquake catalog built on the surface projection of the seismogenic sources (i.e., faults) of the DISS database under the assumption that earthquakes are homogeneously distributed on the seismogenic sources (Fig. 8).

To evaluate the accuracy with which the earthquakes of both catalogs align with the geodetic forecast, thus to check the spatial compatibility of past earthquakes and the active fault with the strain rate map, we utilized the I_1 metric, which is the information score (success) defined by Kagan³⁶ as:

$$I_1 = \frac{1}{n} \sum_{i=1}^n \log_2 \frac{\lambda_i}{\xi} \quad (5)$$

in which n is the number of qualifying test earthquakes, $\lambda_i = \lambda(\vec{x}_i)$ is the seismicity forecast for the cell containing the epicentroid surface point \vec{x}_i , and ξ is the density of a spatially uniform Poissonian process that has the same overall rate of earthquakes. The "success" measure I_1 can be described as the mean information gain (in binary bits) per CPTI15 $m \geq 5.9$ earthquake over an ignorant model with only a single, spatially uniform earthquake rate. The lower the I_1 , the worse the model performance in reproducing the spatial pattern of the earthquake catalog.

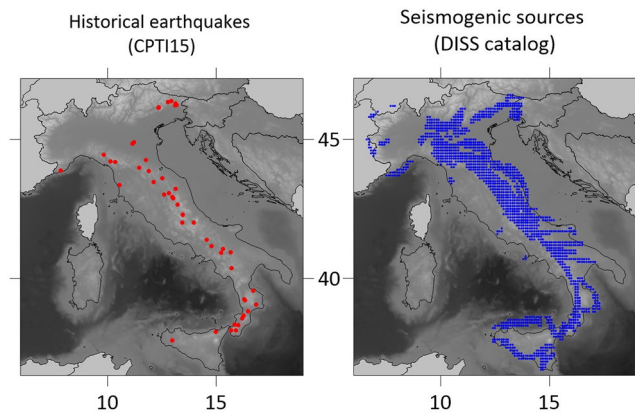


Fig. 8. Tested catalogs. Left: $m \geq 5.9$ historical earthquakes from CPTI15. Right: synthetic earthquakes on the DISS 3.3.0 (DISS Working Group, 2021)³⁰ seismogenic sources.

Influence of strain rate smoothing in I_1 calculations

The selection of the A_0 parameter influences the smoothing of the resulting strain rate map, not its total seismic moment, which is set to \bar{M}_s with the appropriate calculation of $\langle cz \rangle$ in Eq. 4. Thus, the selection of A_0 could potentially affect our findings on the spatial correlation between long-lasting transients following $m \geq 5.9$ earthquakes and strain rate peaks. For this reason, we calculated the seismicity forecast following the approach described in the sub-section "Earthquake forecast from a 2D horizontal strain rate tensor" for all five models listed in Table 1 and presented in Fig. 6 on a grid with a cell spacing of 0.2° . Despite the difference in the strain rate map, the information gains trend in each interval does not change substantially for earthquakes after 1930 AD. Figure 9 shows that the I_1 increase for the latest earthquakes is evident for all models, even though the model with the greatest L_2 -norm misfit to geodetic data ($A_0 = 23 \times 10^7 \text{ m}^2$) has a slightly different pattern for the time interval between 1850 and 1930, likely suggesting an upper limit to the admissible A_0 to be used.

Influence of earthquake position errors and grid spacing in I_1 calculations

CPTI15 earthquakes are reported with variable coordinate errors of 3–8 km for latitude and longitude. We explored the influence of these errors, creating different perturbed catalogs assuming that the reported error describes the 1-sigma uncertainty of earthquake position. We randomly sampled the error of each earthquake position and then investigated the influence of these uncertainties, studying the variation of I_1 standard deviations to the number of used synthetic catalogs. As the seismicity forecast is determined for the cells in which the earthquake falls, we also considered the influence of the grid spacing on the variation of the I_1 standard deviation, finding that in 10 perturbed catalogs, the I_1 standard deviation is stabilized, regardless of the grid spacing.

Once we had fixed the number of testing catalogs to 10, we studied also the influence of the grid spacing in the resulting I_1 trends. In this case, we selected three out of five models presented in subsection "Interseismic strain rate model and Seismic Moment Rate" representing the maximum smoothing of the strain rate ($A_0 = 5 \times 10^7 \text{ m}^2$), maximum fitting to geodetic data ($A_0 = 55 \times 10^7 \text{ m}^2$) and a mean model ($A_0 = 23 \times 10^7 \text{ m}^2$). To magnify the differences among the models, we assigned a grid spacing of 0.3° to the model with maximum smoothing, 0.1° to the model with maximum fitting to the data, and 0.2° to the mean model. The main pattern of I_1 over the

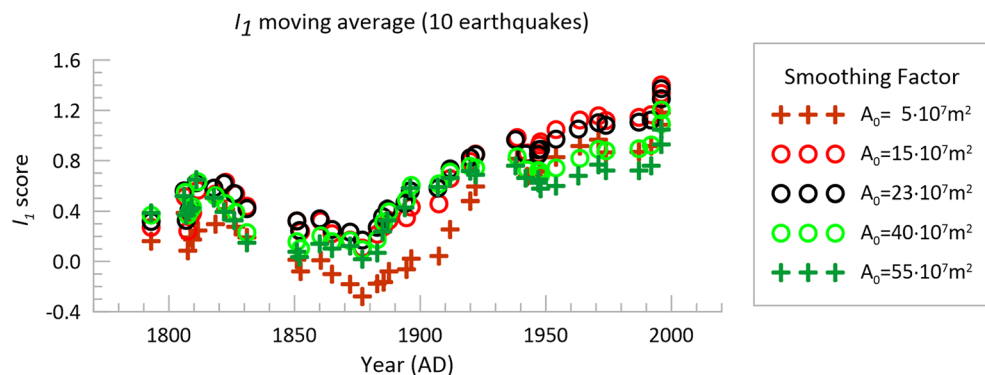


Fig. 9. Influence of the smoothing factor A_0 on the I_1 moving average (10 time-adjacent earthquakes used to compute each point) plotted at the mean year of the considered earthquakes.

investigated years doesn't change, suggesting that the grid spacing and earthquake position errors do not play a significant role in localizing the peak of the strain rates (Fig. 10).

Determining the viscoelastic transient due to the 2009 L'Aquila earthquake

To assess the long-term effects of the 2009 L'Aquila earthquake ($m_w = 6.3$) (Devoti et al.⁴¹ and references therein), we analyzed the time series data from 14 benchmarks equally placed on the hangingwall and footwall. The stations are > 30 km away from the causative fault to avoid the well-known nontectonic transients, such as velocity perturbations due to hydrological changes⁷¹. Our objective was to compare interseismic velocities before and after the earthquake and determine if the observed differences align with the expected lithospheric relaxation from the coseismic impulsive stress. Daily time series fit a linear trend to each benchmark and determine the horizontal velocities relative to the Eurasia reference frame (see Fig. 5).

For cases like the central Apennines, Pollitz (2003, 2005)^{58,72} suggested fitting postseismic velocities within selected time windows to mitigate the influence of unmodeled processes and non-tectonic transients that could skew the model fits. Following this approach, for all GNSS station I , we define for the two geodetic solutions the vectors of velocity difference Δv_k and Δv_j for both the east and north components as

$$\Delta v_k = v_k^{postEQ} - v_k^{preEQ} \tag{6a}$$

$$\Delta v_j = v_j^{postEQ} - v_j^{preEQ} \tag{6b}$$

where v_k^{preEQ}, v_j^{preEQ} are the two horizontal components of the solution anticipating the L'Aquila earthquake and $v_k^{postEQ}, v_j^{postEQ}$ the components in the 2010–2016 period. The correlation matrix defines the uncertainty

$$\tilde{C}_{jk} = \begin{pmatrix} \left(\sigma_{v_{kk}^{postEQ}} \right)^2 + \left(\sigma_{v_{kk}^{preEQ}} \right)^2 & - \left(\frac{\left(\sigma_{v_{jk}^{postEQ}} \right)^2}{\sigma_{v_{kk}^{postEQ}} \cdot \sigma_{v_{kk}^{postEQ}}} + \frac{\left(\sigma_{v_{jk}^{preEQ}} \right)^2}{\sigma_{v_{kk}^{preEQ}} \cdot \sigma_{v_{kk}^{preEQ}}} \right) \\ - \left(\frac{\left(\sigma_{v_{jk}^{postEQ}} \right)^2}{\sigma_{v_{kk}^{postEQ}} \cdot \sigma_{v_{kk}^{postEQ}}} + \frac{\left(\sigma_{v_{jk}^{preEQ}} \right)^2}{\sigma_{v_{kk}^{preEQ}} \cdot \sigma_{v_{kk}^{preEQ}}} \right) & \left(\sigma_{v_{jj}^{postEQ}} \right)^2 + \left(\sigma_{v_{jj}^{preEQ}} \right)^2 \end{pmatrix} \tag{7}$$

whereas the model predictions are indicated with p_k and p_j , accordingly. The velocity misfit function for a given model is then defined as

$$\chi = \sqrt{\frac{\sum_{k=1}^I \sum_{j=1}^I (\Delta v_k - p_k) C_{jk}^{-1} (\Delta v_j - p_j)}{2I}} \tag{8}$$

We calculated postseismic velocities using the PSGRN/PSCMP code^{72,73}, which models a multilayered viscoelastic half-space with elastic parameters derived from seismic velocities and densities as reported by Magnoni et al.⁴⁵. The assumption that the difference between the two velocity solutions can be (at least partially) explained by the viscoelastic response of the lithosphere to the 2009 L'Aquila earthquake is verified by models with $\chi < 1$.

We defined two distinct lithospheric profiles: the first for stations on the western side on the thinner Tyrrhenian lithosphere, comprising an elastic upper crust (0–11 km), a lower crust (11–28 km), and an upper mantle (28–50 km). The second profile is for the thicker Adriatic lithosphere, consisting of an elastic upper crust (0–16 km), a lower crust (16–38 km), and an upper mantle (38–80 km). The PSGRN routine computes time-dependent

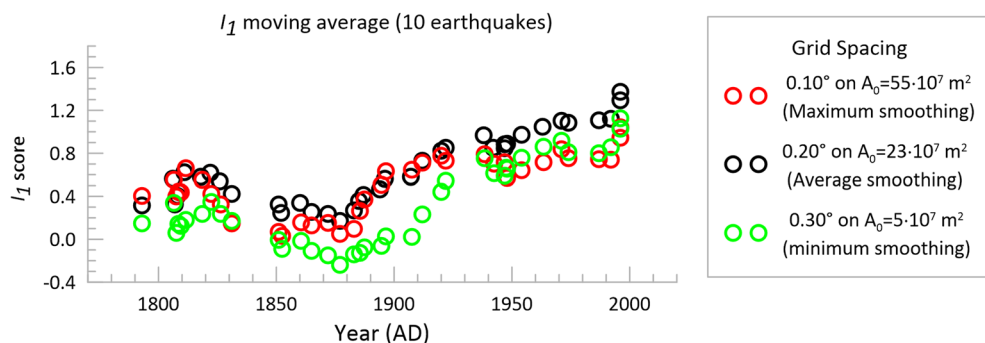


Fig. 10. Influence of grid spacing and earthquake error position on the I_1 moving average (10 earthquakes at each point) plotted at the mean year of the considered earthquakes. The position of each earthquake is perturbed ten times by assuming that the error in longitude and latitude reported in the CPTI15 corresponds to the 1-sigma uncertainty.

Green functions for various dislocation sources at different depths, while PSCMP uses these results to calculate co- and postseismic velocities through linear superposition. We utilized the findings from Ragon et al.⁴⁸ as the source model for the 2009 L'Aquila earthquake.

For both the Tyrrhenian and Adriatic benchmarks, we first tested a Maxwell rheology below an elastic upper crust for both the lower crust and upper mantle. Figure 11 shows that low upper mantle and lower crust viscosities best model the differences between pre- and post-earthquake interseismic velocities with a normalized misfit

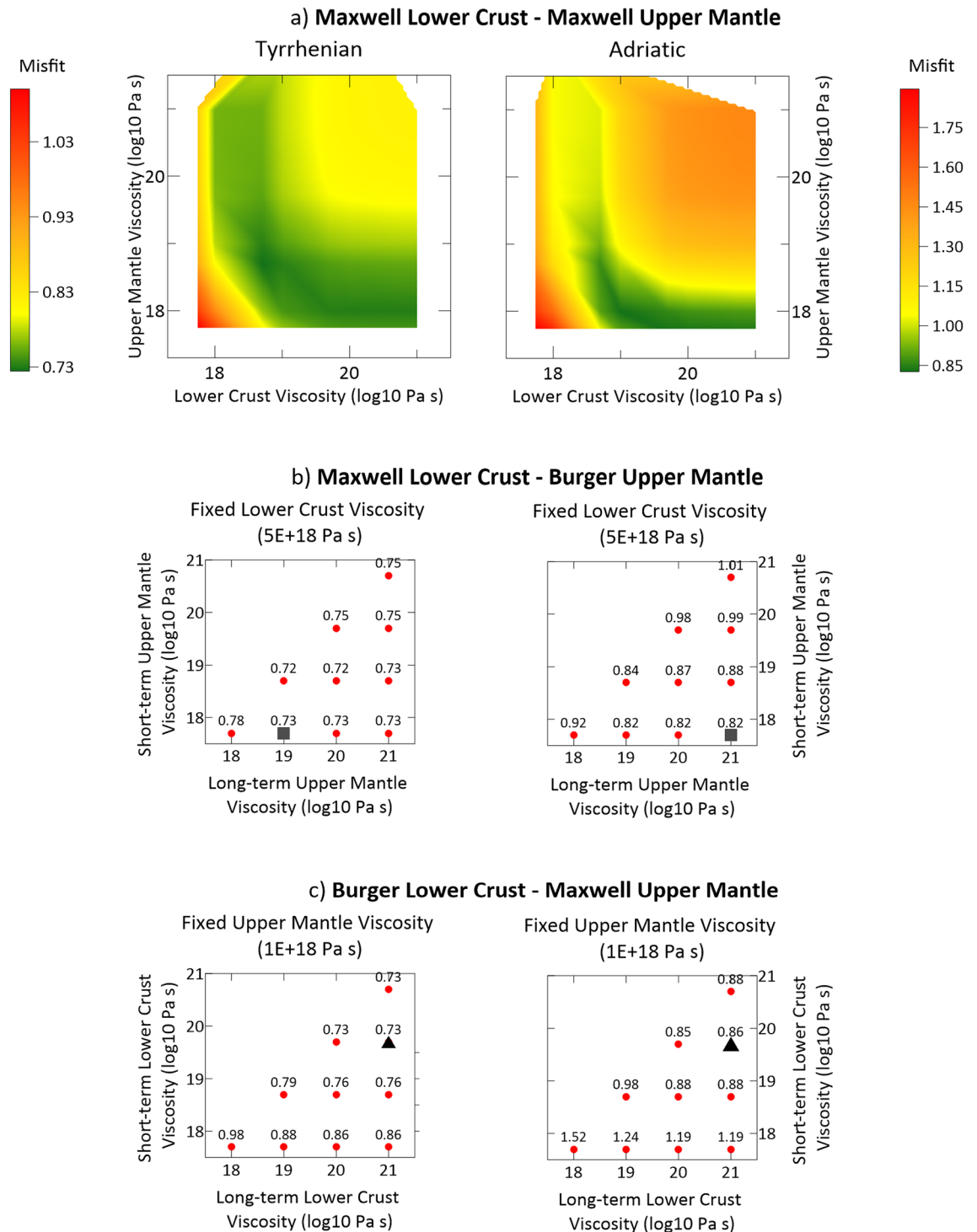


Fig. 11. Viscoelastic relaxation due the L'Aquila 2009 earthquake assuming: (a) a Maxwell viscosity for both lower crust and upper mantle; (b) a Maxwell lower crust and Burger upper mantle; (c) a Burger lower crust and a Maxwell upper mantle. Grey squares in panel (b) define the misfit of the preferred models for both Tyrrhenian and Adriatic benchmarks; Black triangles in panel (c) define the misfit of the alternative viscosity model compared to the preferred one in Fig. 12.

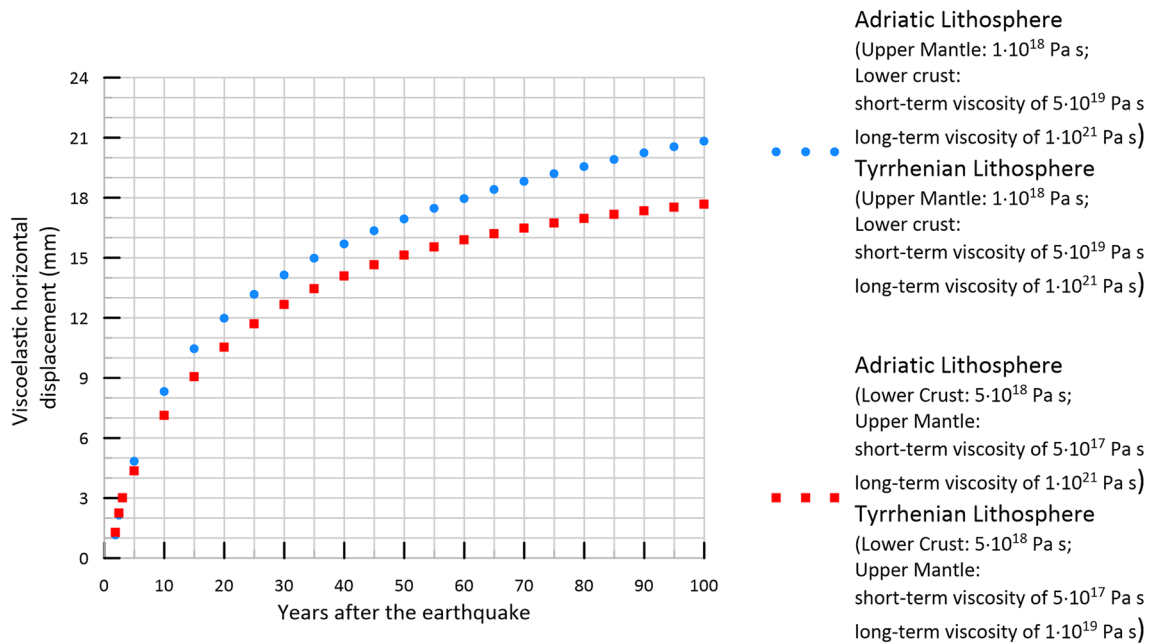


Fig. 12. Comparison of relative displacement due to the viscoelastic relaxation of the lithosphere between two points located 50 km away from the causative fault of the LAquila earthquake. Two alternative viscosity profiles are compared.

of $\chi=0.73$ and $\chi=0.85$. Despite these results, they did not clearly indicate a preferred rheology. Therefore, we explored two other alternative viscosity models for both the Tyrrhenian and Adriatic lithospheres: the first with a fixed Maxwell rheology for the lower crust (viscosity of 5×10^{18} Pa s) and a Burgers rheology with two variable viscosities for the upper mantle; the second with a fixed Maxwell rheology for the upper mantle (viscosity of 1×10^{18} Pa s) and a Burgers rheology with two variable viscosities for the upper mantle. These variations did not conclusively identify a preferred viscosity profile for either side. Nevertheless, across a broad range of lower crust and upper mantle viscosities, the viscoelastic relaxation models have $\chi < 1$ outperforming the most straightforward model, which would attribute the velocity differences to measurement errors corresponding to $\chi=1$.

Based on the geodynamics of the area, we subjectively chose a Burger body as the most suitable viscosity profile for the Tyrrhenian upper mantle (5×10^{17} Pa s for the short-term one and 1×10^{19} Pa s for the long-term one) as well as for the Adriatic ones (5×10^{17} Pa s for the short-term one and 1×10^{21} Pa s for the long-term one). Both lithospheres have a lower crust with a single viscosity of 5×10^{18} Pa s. The normalized misfits for this preferred model are $\chi = 0.72$ for the Tyrrhenian and $\chi = 0.82$ for the Adriatic benchmarks.

To assess the impact of our model choice, we compared the viscoelastic displacement from our preferred model with an alternative one defined as a Maxwell body with uniform viscosity of 1×10^{18} Pa s for both Adriatic and Tyrrhenian upper mantle and Burger body with short-term viscosity of 5×10^{19} Pa s and long-term one of 1×10^{21} Pa s for the lower crust. This model also retained the elastic parameters from Magnoni et al.⁴⁵. The normalized misfits for this alternative model are $\chi = 0.73$ for the Tyrrhenian and $\chi = 0.86$ for the Adriatic benchmarks. Figure 12 compares the long-term displacement expected between two stations located 50 km from the causative fault on both the footwall and the hanging wall for both models. The differences are minor, yet both models predict that the long-term viscoelastic transient will cause an extension rate exceeding 0.2 mm/yr for 30–50 years after the earthquake between these points. Higher extension rates are anticipated at shorter distances, leading to an apparent non-steady localization of the strain rate.

Data availability

The datasets used and/or analysed during the current study are available from the corresponding author on reasonable request.

Received: 31 May 2024; Accepted: 21 August 2024

Published online: 27 August 2024

References

- Bird, P. & Liu, Z. Seismic hazard inferred from tectonics: California. *Seismol. Res. Lett.* **78**, 37–48. <https://doi.org/10.1785/gssrl.78.1.37> (2007).
- Shen, Z. K., Jackson, D. D. & Kagan, Y. Y. Implications of geodetic strain rate for future earthquakes, with a five-year forecast of M5 earthquakes in southern California. *Seismol. Res. Lett.* **78**, 116–120 (2007).
- Bird, P., Kreemer, C. & Holt, W. E. A long-term forecast of shallow seismicity based on the global strain rate map. *Seismol. Res. Lett.* **81**, 184–194. <https://doi.org/10.1785/gssrl.81.2.184> (2010).

4. Bird, P. & Kreemer, C. Revised tectonic forecast of global shallow seismicity based on version 2.1 of the global strain rate map. *Bull. Seismol. Soc. Am.* **105**, 152–166. <https://doi.org/10.1785/0120140129> (2015).
5. Kreemer, C., Holt, W. E. & Haines, A. J. An integrated global model of present-day plate motions and plate boundary deformation. *Geophys. J. Int.* **154**, 8–34. <https://doi.org/10.1046/j.1365-246X.2003.01917.x> (2003).
6. Bird, P., Jackson, D. D., Kagan, Y. Y., Kreemer, C. & Stein, R. S. GEAR1: A global earthquake activity rate model constructed from geodetic strain rates and smoothed seismicity. *Bull. Seismol. Soc. Am.* **105**, 2538–2554. <https://doi.org/10.1785/0120150058> (2015).
7. Strader, A. *et al.* Prospective evaluation of global earthquake forecast models: 2 yrs of observations provide preliminary support for merging smoothed seismicity with geodetic strain rates. *Seismol. Res. Lett.* **89**, 1262–1271. <https://doi.org/10.1785/0220180051> (2018).
8. Bayona, J. A. *et al.* Are regionally calibrated seismicity models more informative than global models? Insights from California, New Zealand, and Italy. *Seismic Record* **3**, 86–95. <https://doi.org/10.1785/0320230006> (2023).
9. Carafa, M. M. C., Valensise, G. & Bird, P. Assessing the seismic coupling of shallow continental faults and its impact on seismic hazard estimates: A case-study from Italy. *Geophys. J. Int.* **209**, 32–47. <https://doi.org/10.1093/gji/ggx002> (2017).
10. Stevens, V. L. & Avouac, J. P. On the relationship between strain rate and seismicity in the India-Asia collision zone: Implications for probabilistic seismic hazard. *Geophys. J. Int.* **226**, 220–245. <https://doi.org/10.1093/gji/ggab098> (2021).
11. Zheng, G., Lou, Y., Wang, H., Geng, J. & Shi, C. Shallow seismicity forecast for the india- Eurasia collision zone based on geodetic strain rates. *Geophys. Res. Lett.* **45**, 8905–8912. <https://doi.org/10.1029/2018gl078814> (2018).
12. Wei, C.-M. *et al.* Time-independent grid-based forecast model for $M \geq 6.0$ Earthquakes in southeastern tibetan plateau using gnss strain rates and seismicity. *Bull. Seismol. Soc. Am.* <https://doi.org/10.1785/0120230152> (2023).
13. Nishimura, T. Time-independent forecast model for large crustal earthquakes in southwest Japan using GNSS data. *Earth Planets Space* **74**, 58. <https://doi.org/10.1186/s40623-022-01622-5> (2022).
14. Maurer, J. *et al.* Geodetic strain rates for the 2022 update of the New Zealand national seismic hazard model. *Bull. Seismol. Soc. Am.* <https://doi.org/10.1785/0120230145> (2023).
15. Maurer, J. & Materna, K. Quantification of geodetic strain rate uncertainties and implications for seismic hazard estimates. *Geophys. J. Int.* **234**, 2128–2142. <https://doi.org/10.1093/gji/ggad191> (2023).
16. Bürgmann, R. & Dresen, G. Rheology of the lower crust and upper mantle: Evidence from rock mechanics, geodesy, and field observations. *Annu. Rev. Earth Planet. Sci.* <https://doi.org/10.1146/annurev.earth.36.031207.124326> (2008).
17. Doglioni, C., Barba, S., Carminati, E. & Riguzzi, F. Role of the brittle–ductile transition on fault activation. *Phys. Earth Planetary Interiors* **184**, 160–171. <https://doi.org/10.1016/j.pepi.2010.11.005> (2011).
18. Bird, P. Plate-tectonic analysis of shallow seismicity: Apparent boundary width, beta, corner magnitude, coupled lithosphere thickness, and coupling in seven tectonic settings. *Bull. Seismol. Soc. Am.* **94**, 2380–2399. <https://doi.org/10.1785/0120030107> (2004).
19. Hearn, E. H., Pollitz, F. F., Thatcher, W. R. & Onishi, C. T. How do “ghost transients” from past earthquakes affect GPS slip rate estimates on southern California faults?. *Geochem. Geophys. Geosyst.* **14**, 828–838. <https://doi.org/10.1002/ggge.20080> (2013).
20. Thatcher, W. Nonlinear strain buildup and the earthquake cycle on the San Andreas Fault. *J. Geophys. Res.: Solid Earth* **88**, 5893–5902. <https://doi.org/10.1029/JB088iB07p05893> (1983).
21. Hearn, E. “Ghost transient” corrections to the southern California GPS velocity field from san andreas fault seismic cycle models. *Seismol. Res. Lett.* **93**, 2973–2989. <https://doi.org/10.1785/0220220156> (2022).
22. Pollitz, F. F. *et al.* Western U.S. deformation models for the 2023 update to the U.S. national seismic hazard model. *Seismol. Res. Lett.* **93**, 3068–3086. <https://doi.org/10.1785/0220220143> (2022).
23. Johnson, K. M., Hammond, W. C. & Weldon, R. J. Review of geodetic and geologic deformation models for 2023 U.S. national seismic hazard model. *Bull. Seismol. Soc. Am.* <https://doi.org/10.1785/0120230137> (2024).
24. Carafa, M. M. C. *et al.* Partitioning the ongoing extension of the central apennines (Italy): Fault slip rates and bulk deformation rates from geodetic and stress data. *J. Geophys. Res.: Solid Earth* <https://doi.org/10.1029/2019JB018956> (2020).
25. Serpelloni, E. *et al.* Surface velocities and strain-rates in the euro-mediterranean region from massive GPS data processing. *Front. Earth Sci.* <https://doi.org/10.3389/feart.2022.907897> (2022).
26. Carafa, M. M. C. & Bird, P. Improving deformation models by discounting transient signals in geodetic data: 2. Geodetic data, stress directions, and long-term strain rates in Italy. *J. Geophys. Res.: Solid Earth* **121**, 5557–5575. <https://doi.org/10.1002/2016JB013038> (2016).
27. Serpelloni, E., Vannucci, G., Anderlini, L. & Bennett, R. A. Kinematics, seismotectonics and seismic potential of the eastern sector of the European Alps from GPS and seismic deformation data. *Tectonophysics* **688**, 157–181. <https://doi.org/10.1016/j.tecto.2016.09.026> (2016).
28. Rovida, A., Locati, M., Camassi, R., Lolli, B. & Gasperini, P. The Italian earthquake catalogue CPTI15. *Bull. Earthq. Eng.* **18**, 2953–2984. <https://doi.org/10.1007/s10518-020-00818-y> (2020).
29. Meletti, C. *et al.* The new Italian seismic hazard model (MPS19). *Ann. Geophys.* <https://doi.org/10.4401/ag-8579> (2021).
30. DISS Working Group. Database of Individual Seismogenic Sources (DISS), Version 3.3.0: A compilation of potential sources for earthquakes larger than $M 5.5$ in Italy and surrounding areas. <https://doi.org/10.13127/diss3.3.0> (2021).
31. King, G. C. P., Stein, R. S. & Lin, J. Static stress changes and the triggering of earthquakes. *Bull. Seismol. Soc. Am.* **84**, 935–953. <https://doi.org/10.1785/bssa0840030935> (1994).
32. Bird, P. & Carafa, M. M. C. Improving deformation models by discounting transient signals in geodetic data: 1. Concept and synthetic examples. *J. Geophys. Res.: Solid Earth* **121**, 5538–5556. <https://doi.org/10.1002/2016JB013056> (2016).
33. Mariucci, M. T. & Montone, P. Database of Italian present-day stress indicators, IPSI 1.4. *Sci Data* **7**, 298. <https://doi.org/10.1038/s41597-020-00640-w> (2020).
34. Carafa, M. M. C. & Bird, P. Improving deformation models by discounting transient signals in geodetic data: 2. Geodetic data, stress directions, and long-term strain rates in Italy. *J. Geophys. Res.: Solid Earth* **121**, 5557–5575. <https://doi.org/10.1002/2016JB013038> (2016).
35. Kagan, Y. Y. Seismic moment distribution revisited: II. Moment conservation principle. *Geophys. J. Int.* **149**, 731–754. <https://doi.org/10.1046/j.1365-246X.2002.01671.x> (2002).
36. Kagan, Y. Y. Testing long-term earthquake forecasts: Likelihood methods and error diagrams. *Geophys. J. Int.* **177**(2), 532–542. <https://doi.org/10.1111/j.1365-246X.2008.04064.x> (2009).
37. Bird, P. An updated digital model of plate boundaries. *Geochem. Geophys. Geosyst.* **4**, 1–52. <https://doi.org/10.1029/2001gc000252> (2003).
38. Carafa, M. M. C., Di Naccio, D., Di Lorenzo, C., Kastelic, V. & Bird, P. A Meta-analysis of fault slip rates across the central apennines. *J. Geophys. Res.-Solid Earth* **127**, e2021JB023252. <https://doi.org/10.1029/2021JB023252> (2022).
39. Cheloni, D. *et al.* Coseismic and post-seismic slip of the 2009 LAquila (central Italy) MW 6.3 earthquake and implications for seismic potential along the Campotosto fault from joint inversion of high-precision levelling, InSAR and GPS data. *Tectonophysics* **622**, 168–185. <https://doi.org/10.1016/j.tecto.2014.03.009> (2014).
40. Gualandi, A., Serpelloni, E. & Belardinelli, M. E. Space–time evolution of crustal deformation related to the Mw 6.3, 2009 LAquila earthquake (central Italy) from principal component analysis inversion of GPS position time-series. *Geophys. J. Int.* **197**, 174–191. <https://doi.org/10.1093/gji/ggt522> (2014).
41. Devoti, R. *et al.* The coseismic and postseismic deformation of the LAquila, 2009 earthquake from repeated GPS measurements. *Ital. J. Geosci.* **131**, 348–358. <https://doi.org/10.3301/IJG.2012.15> (2012).

42. Doglioni, C., Merlini, S. & Cantarella, G. Foredeep geometries at the front of the Apennines in the Ionian Sea (central Mediterranean). *Earth Planetary Sci. Lett.* **168**, 243–254 (1999).
43. Faccenna, C. & Becker, T. W. History of subduction and back arc extension in the central Mediterranean. *Geophys. J. Int.* **145**(3), 809–820 (2001).
44. Doglioni, C. A proposal for the kinematic modeling of W-dipping subductions - possible applications to the tyrrhenian apennines system. *Terra Nova* **3**, 423–434. <https://doi.org/10.1111/j.1365-3121.1991.tb00172.x> (1991).
45. Magnoni, F. *et al.* Adjoint tomography of the Italian lithosphere. *Commun. Earth Environ.* **3**, 69 (2022).
46. Devoti, R., Pietrantonio, G., Pisani, A. R., Riguzzi, F. & Serpelloni, E. Present day kinematics of Italy. *J. Virtual Explor.* <https://doi.org/10.3809/jvirtex.2010.00237> (2010).
47. Devoti, R., Esposito, A., Pietrantonio, G., Pisani, A. R. & Riguzzi, F. Evidence of large scale deformation patterns from GPS data in the Italian subduction boundary. *Earth Planetary Sci. Lett.* **311**, 230–241. <https://doi.org/10.1016/j.epsl.2011.09.034> (2011).
48. Ragon, T. *et al.* Joint inversion of coseismic and early postseismic slip to optimize the information content in geodetic data: Application to the 2009 6.3 L'Aquila Earthquake, Central Italy. *J. Geophys. Res.-Solid Earth* **124**, 10522–10543. <https://doi.org/10.1029/2018jb017053> (2019).
49. Ingleby, T. & Wright, T. J. Omori-like decay of postseismic velocities following continental earthquakes. *Geophys. Res. Lett.* **44**, 3119–3130. <https://doi.org/10.1002/2017GL072865> (2017).
50. Mavrommatis, A. P., Segall, P. & Johnson, K. M. A decadal-scale deformation transient prior to the 2011 Mw 9.0 Tohoku-oki earthquake. *Geophys. Res. Lett.* **41**, 4486–4494. <https://doi.org/10.1002/2014gl060139> (2014).
51. Loveless, J. P. & Meade, B. J. Two decades of spatiotemporal variations in subduction zone coupling offshore Japan. *Earth Planetary Sci. Lett.* **436**, 19–30. <https://doi.org/10.1016/j.epsl.2015.12.033> (2016).
52. DeVries, P. M. R., Krastev, P. G., Dolan, J. F. & Meade, B. J. Viscoelastic block models of the north Anatolian fault: A unified earthquake cycle representation of pre- and postseismic geodetic observations. *Bull. Seismol. Soc. Am.* **107**, 403–417. <https://doi.org/10.1785/0120160059> (2017).
53. Frost, E., Dolan, J., Ratschbacher, L., Hacker, B. & Seward, G. Direct observation of fault zone structure at the brittle-ductile transition along the Salzach-Ennstal-Mariazell-Puchberg fault system, Austrian Alps. *J. Geophys. Res.: Solid Earth* <https://doi.org/10.1029/2010JB007719> (2011).
54. Hanmer, S. Great Slave Lake Shear Zone, Canadian Shield: Reconstructed vertical profile of a crustal-scale fault zone. *Tectonophysics* **149**, 245–264. [https://doi.org/10.1016/0040-1951\(88\)90176-X](https://doi.org/10.1016/0040-1951(88)90176-X) (1988).
55. Norris, R. J. & Cooper, A. F. Very high strains recorded in mylonites along the Alpine Fault, New Zealand: Implications for the deep structure of plate boundary faults. *J. Struct. Geol.* **25**, 2141–2157. [https://doi.org/10.1016/S0191-8141\(03\)00045-2](https://doi.org/10.1016/S0191-8141(03)00045-2) (2003).
56. Vauchez, A. & Tommasi, A. Wrench faults down to the asthenosphere: Geological and geophysical evidence and thermomechanical effects. *Geol. Soc. Lond. Spec. Publ.* **210**, 15–34. <https://doi.org/10.1144/GSL.SP.2003.210.01.02> (2003).
57. Freed, A. M., Bürgmann, R., Calais, E., Freymueller, J. & Hreinsdóttir, S. Implications of deformation following the 2002 Denali, Alaska, earthquake for postseismic relaxation processes and lithospheric rheology. *J. Geophys. Res.: Solid Earth* <https://doi.org/10.1029/2005JB003894> (2006).
58. Pollitz, F. F. Transient rheology of the uppermost mantle beneath the Mojave Desert, California. *Earth Planetary Sci. Lett.* **215**, 89–104. [https://doi.org/10.1016/S0012-821X\(03\)00432-1](https://doi.org/10.1016/S0012-821X(03)00432-1) (2003).
59. Ryder, I., Parsons, B., Wright, T. J. & Funning, G. J. Post-seismic motion following the 1997 Manyi (Tibet) earthquake: InSAR observations and modelling. *Geophys. J. Int.* **169**, 1009–1027. <https://doi.org/10.1111/j.1365-246X.2006.03312.x> (2007).
60. Mandler, E. *et al.* Post-seismic deformation related to the 2016 Central Italy seismic sequence from GPS displacement time-series. *J. Geophys. Res.: Solid Earth* **126**, e2021JB022200. <https://doi.org/10.1029/2021JB022200> (2021).
61. D'Agostino, N. Complete seismic release of tectonic strain and earthquake recurrence in the Apennines (Italy). *Geophys. Res. Lett.* **41**, 1155–1162. <https://doi.org/10.1002/2014gl059230> (2014).
62. Bird, P. Long-term fault slip rates, distributed deformation rates, and forecast of seismicity in the western United States from joint fitting of community geologic, geodetic, and stress direction data sets. *J. Geophys. Res.: Solid Earth* <https://doi.org/10.1029/2009jb006317> (2009).
63. Carafa, M. M. C., Kastelic, V., Bird, P., Maesano, F. E. & Valensise, G. A “Geodetic Gap” in the Calabrian Arc: Evidence for a locked subduction megathrust?. *Geophys. Res. Lett.* **45**, 1794–1804. <https://doi.org/10.1002/2017gl076554> (2018).
64. Ghadimi, H., Khodaverdian, A. & Zafarani, H. Active deformation in the Makran region using geological, geodetic and stress direction data sets. *Geophys. J. Int.* **235**, 2556–2580. <https://doi.org/10.1093/gji/ggad393> (2023).
65. Taroni, M. & Carafa, M. M. C. Earthquake size distributions are slightly different in compression vs extension. *Commun. Earth Environ.* **4**, 398. <https://doi.org/10.1038/s43247-023-01059-y> (2023).
66. Carafa, M. M. C. & Barba, S. The stress field in Europe: optimal orientations with confidence limits. *Geophys. J. Int.* **193**, 531–548. <https://doi.org/10.1093/gji/ggt024> (2013).
67. Carafa, M. M. C., Tarabusi, G. & Kastelic, V. SHINE: Web application for determining the horizontal stress orientation. *Comput. Geosci.* **74**, 39–49. <https://doi.org/10.1016/j.cageo.2014.10.001> (2015).
68. Bird, P. & Li, Y. Interpolation of principal stress directions by nonparametric statistics: Global maps with confidence limits. *J. Geophys. Res.-Solid Earth* **101**, 5435–5443. <https://doi.org/10.1029/95jb03731> (1996).
69. Kijko, A. & Sellevoll, M. A. Estimation of earthquake hazard parameters for incomplete and uncertain data files. *Nat. Hazards* **3**, 1–13. <https://doi.org/10.1007/bf00144970> (1990).
70. Taroni, M. & Selva, J. GR_EST: An OCTAVE/MATLAB toolbox to estimate Gutenberg-Richter law parameters and their uncertainties. *Seismol. Res. Lett.* **92**, 508–516. <https://doi.org/10.1785/0220200028> (2020).
71. Devoti, R., Riguzzi, F., Cinti, F. R. & Ventura, G. Long-term strain oscillations related to the hydrological interaction between aquifers in intra-mountain basins: A case study from Apennines chain (Italy). *Earth Planetary Sci. Lett.* **501**, 1–12. <https://doi.org/10.1016/j.epsl.2018.08.014> (2018).
72. Pollitz, F. F. Transient rheology of the upper mantle beneath central Alaska inferred from the crustal velocity field following the 2002 Denali earthquake. *J. Geophys. Res.-Solid Earth* <https://doi.org/10.1029/2005jb003672> (2005).
73. Wang, R. J., Lorenzo-Martin, F. & Roth, F. PSGRN/PSCMP -: A new code for calculating co- and post-seismic deformation, geoid and gravity changes based on the viscoelastic-gravitational dislocation theory. *Comput. Geosci.* **32**, 527–541. <https://doi.org/10.1016/j.cageo.2005.08.006> (2006).

Acknowledgements

We would like to thank the Editor (Prof. Irene di Palma), Prof. Brendan Meade, and one anonymous reviewer for their valuable comments and suggestions. We would like to thank Federica Riguzzi and the GNSS Data Analysis Center at the INGV for providing the daily solutions obtained with the Bernese software. MMCC has been partially funded by the call PRIN2022PNRR, code P2022P37SN - project ‘RELATION BETWEEN 3D THERMO-RHEOLOGICAL MODEL AND SEISMIC HAZARD FOR THE RISK MITIGATION IN THE URBAN AREAS OF SOUTHERN ITALY (TRHAM)’, Decree of Admission to funding - Director decree no. 1388 of 01/09/2023, ERC sector PE10 ‘EARTH SYSTEM SCIENCE, FUNDED BY THE EUROPEAN UNION - NEXT

GENERATION EU'; MT has been partially funded by the call PRIN2022, code 2022TAFXZ5 - project 'Artificial Intelligence and STOchastic simulation for the rESilience of critical infrastruCTurES (ARISTOTELES)', Decree of Admission to funding - Director decree no. 960 of 30/06/2023, ERC sector PE7 'EARTH SYSTEM SCIENCE, FUNDED BY THE EUROPEAN UNION - NEXT GENERATION EU'.

Author contributions

Conceptualization: Ideas; formulation or evolution of overarching research goals and aims. Contributors: M.C., C.D., P.B. **Methodology:** Development or design of methodology; creation of models. Contributors: M.C., P.B. **Software:** Programming, software development; designing computer programs; implementation of the computer code and supporting algorithms; testing of existing code components. Contributor: P.B. **Validation:** Verification, whether as a part of the activity or separate, of the overall replication/reproducibility of results/experiments and other research outputs. Contributors: M.C., M.T., A.V., P.B. **Formal analysis:** Application of statistical, mathematical, computational, or other formal techniques to analyze or synthesize study data. Contributors: M.C., P.B., A.V., M.T. **Investigation:** Conducting a research and investigation process, specifically performing the experiments, or data/evidence collection. Contributors: M.C., A.V., M.T. **Writing—Original Draft:** Preparation, creation, and/or presentation of the published work, specifically writing the initial draft (including substantive translation). Contributor: M.C. **Writing—Review & Editing:** Preparation, creation, and/or presentation of the published work by those from the original research group, specifically critical review, commentary, or revision—including pre- or post-publication stages. Contributors: M.C., P.B., A.V., M.T., C.D. **Funding acquisition:** Acquisition of the financial support for the project leading to this publication. Contributors: M.C., M.T., C.D.

Competing interests

The authors declare no competing interests.

Additional information

Correspondence and requests for materials should be addressed to M.M.C.C.

Reprints and permissions information is available at www.nature.com/reprints.

Publisher's note Springer Nature remains neutral with regard to jurisdictional claims in published maps and institutional affiliations.

Open Access This article is licensed under a Creative Commons Attribution-NonCommercial-NoDerivatives 4.0 International License, which permits any non-commercial use, sharing, distribution and reproduction in any medium or format, as long as you give appropriate credit to the original author(s) and the source, provide a link to the Creative Commons licence, and indicate if you modified the licensed material. You do not have permission under this licence to share adapted material derived from this article or parts of it. The images or other third party material in this article are included in the article's Creative Commons licence, unless indicated otherwise in a credit line to the material. If material is not included in the article's Creative Commons licence and your intended use is not permitted by statutory regulation or exceeds the permitted use, you will need to obtain permission directly from the copyright holder. To view a copy of this licence, visit <http://creativecommons.org/licenses/by-nc-nd/4.0/>.

© The Author(s) 2024, corrected publication 2024